Electronic Supplementary Material (ESI) for Materials Advances.

First-principles modelling of the thermoelectric properties of n-type $CaTiO_3$, $SrTiO_3$ and $BaTiO_3$: Electronic supplementary information

Alveena Z. Khan, Joseph M. Flitcroft, and Jonathan M. Skelton

1 Comparison of calculations on $SrTiO_3$ to experiments on single crystals

To assess the accuracy of our predicted figures of merit ZT and constituent properties, *viz.* the electrical conductivity σ, Seebeck coefficient S, and thermal conductivity κ, for $SrTiO_3$, we compared our calculations to the measurements on the four doped single-crystal $SrTiO_3$ samples reported in Ref. [1]. While this study does not confirm the phase of the crystals, the transition between the low-temperature tetragonal and high-temperature cubic phases of STO occurs below room temperature (around 100 K),[2] and we would therefore expect the crystals to be in the cubic structure for all of the reported measurements. In this case, the electrical and thermal transport properties and the ZT are isotropic, and the most sensible comparison is to our predicted averaged values.

Fig. S1 compares the measured κ_{latt} as a function of temperature for the four experimental samples (Samples (a)-(d)) to our calculations. We find that the predictions are generally a factor of two smaller than the measured values, which we put down to the expected higher thermal conductivity of the cubic phase compared to the tetragonal phase.

Fig. S2 compares the measured σ and S as a function of temperature for the four experimental samples to the averaged values predicted at the different carrier concentrations n we tested in the calculations. The measurements fall within the ranges of the predicted values, but in general cannot be reproduced by a single value of n. We therefore performed a 2D interpolation of the predicted $\sigma(n,T)$ and $S(n,T)$ and used this in conjunction with a fitting algorithm to estimate the n required to reproduce the measured properties in the calculations. Fig. S3(a) and (c) compare the fitted and measured σ and S, confirming that both are superimposable, and Fig. S3(b) and (d) compare the n required to reproduce the measurements to the experimental doping levels. This comparison indicates that the calculations typically over- and underestimate the n required to obtain a given conductivity at low and high T, respectively, and underestimate the n required to obtain a given Seebeck coefficient. Equivalently, for a given value of n, the calculations are likely to under- or overestimate the σ at low and high temperature, respectively, but are likely to overestimate the S, given the predicted monotonic reduction in S with carrier concentration.

To better quantify these discrepancies, Table S1 compares the experimental doping levels to the fitted n required to reproduce the σ and S at T = 400, 600 and 1000 K. The calculations overestimate the n required to reproduce the measured conductivity at 400 K by 1.08-1.28 $\times$ and underestimate it by a factor of 1.5-3 $\times$ at 1000 K, and underestimate the carrier concentration required to reproduce the measured S by a factor of 1.5-4, with no obvious temperature trend.

There are a number of possible explanations for this discrepancy. Firstly, the higher valley degeneracy in the cubic phase would likely increase the Seebeck coefficient compared to the tetragonal phase. If this is the case, and if the S shows a similar monotonic decrease with carrier concentration in the cubic phase, we would expect a larger S for a given carrier concentration, and this is consistent with the discrepancy between the measured and fitted n. Secondly, it has been shown that the grain boundaries in more typical thin film or pressed/sintered pellet samples can result in a mixture of "energy filtering" and "carrier pocketing", both of which impact upon the electrical properties.[3] While we would not expect grain-boundary effects to be prominent in single crystals, we might expect the point defects introduced by large dopant concentrations to produce similar phenomena. Finally, these calculations are performed within the rigid-band approximation,[4] which may not be valid at the high doping levels in the experiments.

Nevertheless, the predicted n required to obtain a given electrical conductivity or Seebeck coefficient are invariably within an order of magnitude of the measured n, which, in our view, constitutes useful accuracy.

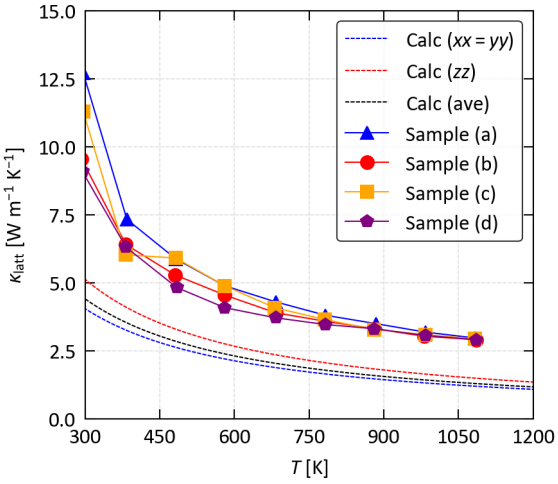

Fig. S1 Comparison of the calculated lattice thermal conductivity κ_{latt} of $SrTiO_3$ (dashed lines) to the measured κ_{latt} of the four single-crystal $SrTiO_3$ samples reported in Ref. [1] (Samples (a)-(d); solid lines with markers). The principal $xx = yy$ and zz components of the calculated $\boldsymbol{\kappa}_{\text{latt}}$ tensors are shown together with the scalar average $(xx+yy+zz)/3$.

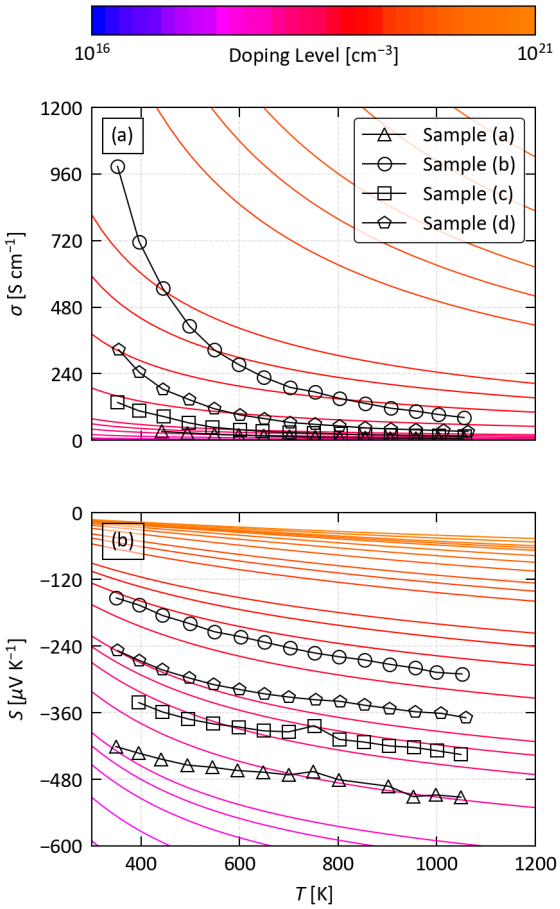

Fig. S2 Comparison of the calculated averaged electrical conductivity σ (a) and Seebeck coefficient S (b) of $SrTiO_3$ as a function of temperature and doping level (coloured lines) to the measured values for the four single-crystal $SrTiO_3$ samples reported in Ref. [1] (Samples (a)-(d); black lines with markers).

			Fit (σ)		Fit (S)	
	T [K]	Expt n [cm^{-3}]	Calc. n [cm^{-3}]	$\Delta[\times]$	Calc. n [cm^{-3}]	$\Delta[\times]$
Sample (a)	400	5×10^{19}	6.4×10^{19}	1.28	1.3×10^{19}	0.26
	600		4.8×10^{19}	0.97	2.1×10^{19}	0.41
	1000		3×10^{19}	0.6	2.6×10^{19}	0.52
Sample (b)	400	6.8×10^{20}	1.1×10^{21}	1.62	4.4×10^{20}	0.65
	600		6.8×10^{20}	0.99	4×10^{20}	0.58
	1000		3.7×10^{20}	0.54	3.5×10^{20}	0.51
Sample (c)	400	1.5×10^{20}	1.7×10^{20}	1.12	3.9×10^{19}	0.26
	600		1×10^{20}	0.67	5.2×10^{19}	0.35
	1000		6.7×10^{19}	0.45	6.6×10^{19}	0.44
Sample (d)	400	3.7×10^{20}	4×10^{20}	1.08	1×10^{20}	0.28
	600		2.3×10^{20}	0.63	1.2×10^{20}	0.32
	1000		1.3×10^{20}	0.36	1.5×10^{20}	0.4

Table S1 Summary of the results obtained by fitting the measured electrical conductivity σ and Seebeck coefficient S of the four $SrTiO_3$ samples reported in Ref. [1] (Samples (a)-(d)) at T = 400, 600 and 1000 K to electrical-transport calculations. For each of the four samples and three temperatures we show the experimental doping levels, the carrier concentrations n estimated by fitting the experimental properties, and the ratio between the fitted and experimental values.

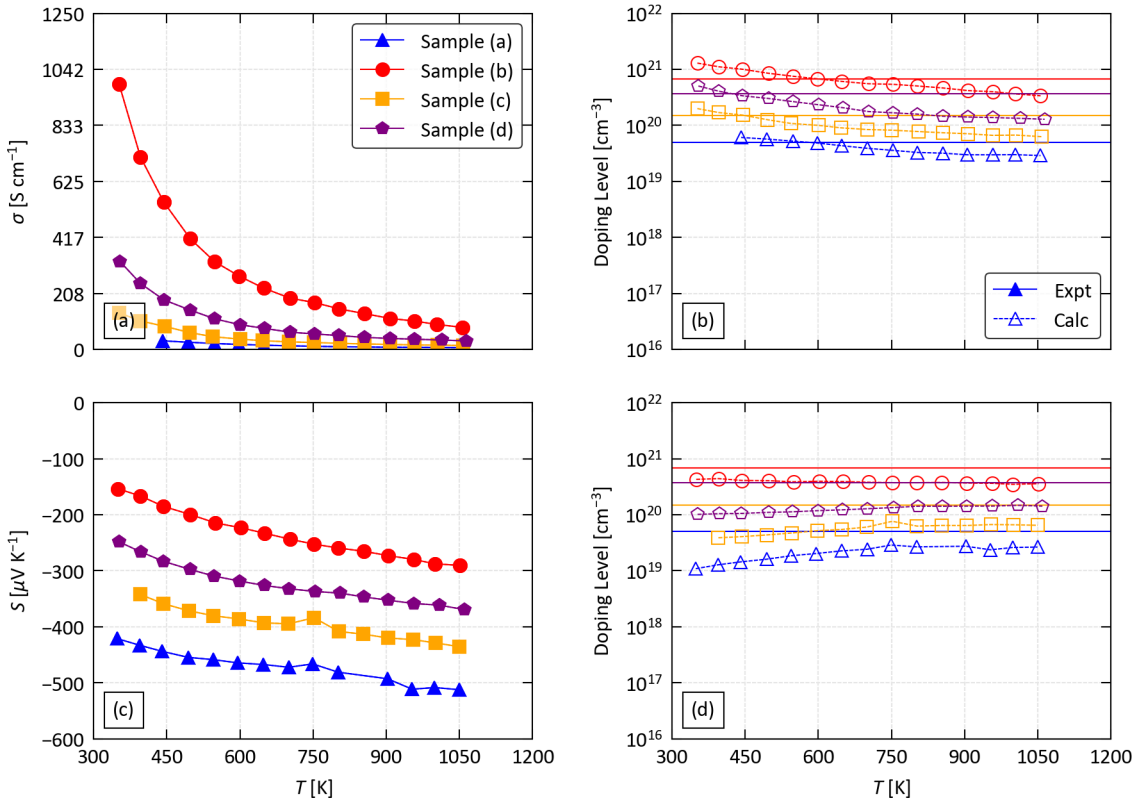

Fig. S3 Comparison of the measured electrical conductivity σ (a/b) and Seebeck coefficient S (c/d) of the four single-crystal $SrTiO_3$ samples reported in Ref. [1] (Samples (a)-(d)) to electrical-transport calculations. The plots in the left-hand column (a/c) compare the measurements (solid lines/filled markers) to the values obtained from the calculations with best-fit values of n (hollow markers/dashed lines). The plots in the right-hand column (b/d) compare the best-fit values of n (hollow markers/dashed lines) to the experimental doping levels (solid lines).

2 Supplementary figures and tables

2.1 Anisotropy in the lattice thermal conductivity

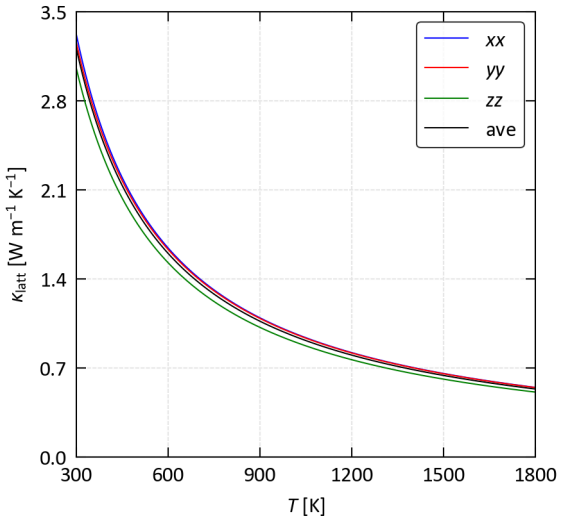

Fig. S4 Calculated lattice thermal conductivity κ_{latt} of $CaTiO_3$ as a function of temperature. The plot shows the principal xx, yy and zz elements of the $\boldsymbol{\kappa}_{\text{latt}}$ tensor, together with the scalar average $(xx+yy+zz)/3$ discussed in the manuscript.

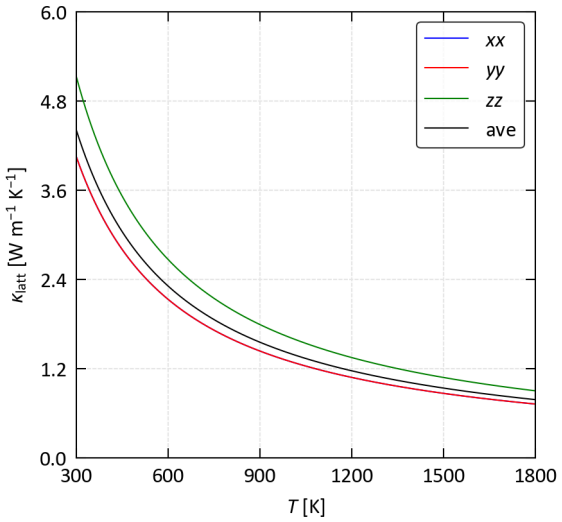

Fig. S5 Calculated lattice thermal conductivity κ_{latt} of $SrTiO_3$ as a function of temperature. The plot shows the principal xx, yy and zz elements of the $\boldsymbol{\kappa}_{\text{latt}}$ tensor, together with the scalar average $(xx+yy+zz)/3$ discussed in the manuscript.

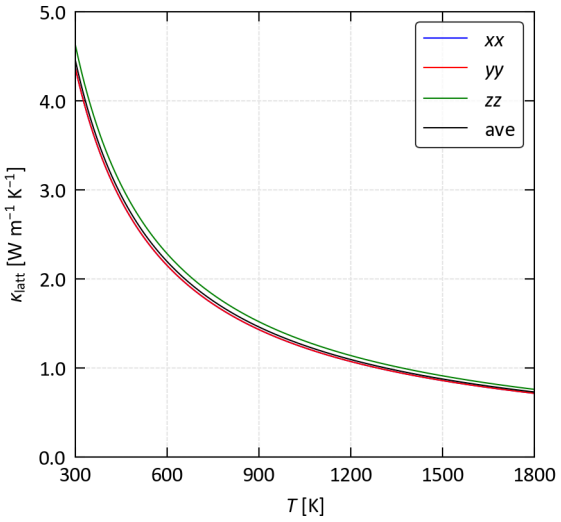

Fig. S6 Calculated lattice thermal conductivity κ_{latt} of $BaTiO_3$ as a function of temperature. The plot shows the principal xx, yy and zz elements of the $\boldsymbol{\kappa}_{\mathrm{latt}}$ tensor, together with the scalar average $(xx+yy+zz)/3$ discussed in the manuscript.

2.2 Electronic band structures and density of states curves

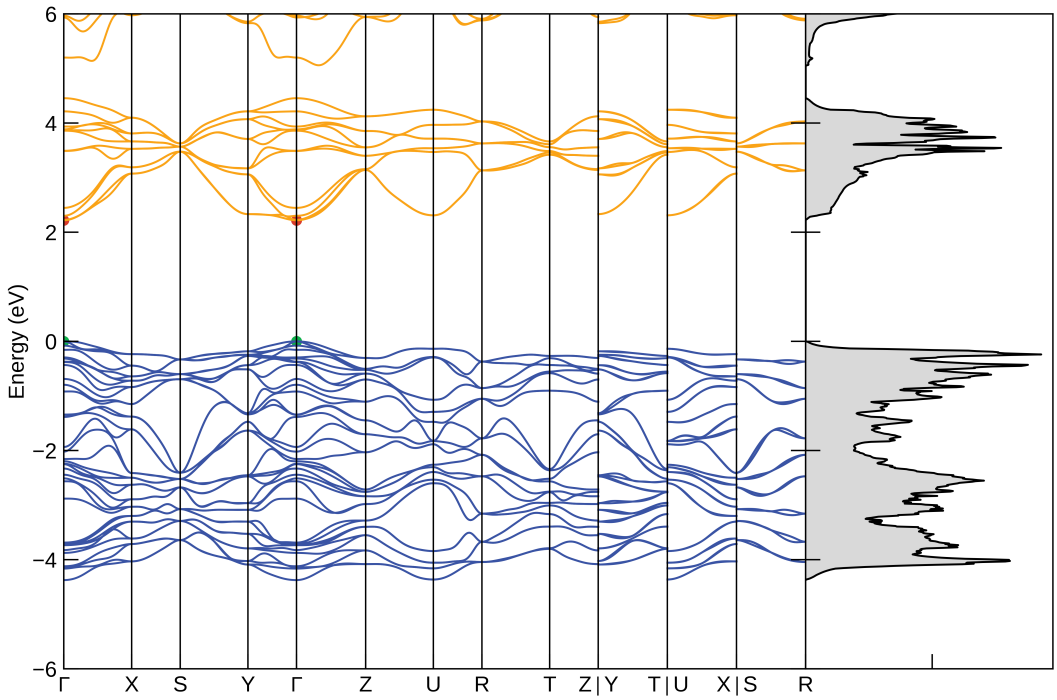

Fig. S7 Calculated electronic band structure and density of states (DoS) of $CaTiO_3$ obtained with the PBEsol exchange-correlation functional. The valence and conduction bands are shown in blue and orange, respectively, the valence-band maximum and conduction-band minimum (VBM/CBM) are marked by green and red circles, and the VBM is set to $E = 0$. Note that the PBEsol bandgap shown on these plots is smaller than the HSE06 values given in the paper.

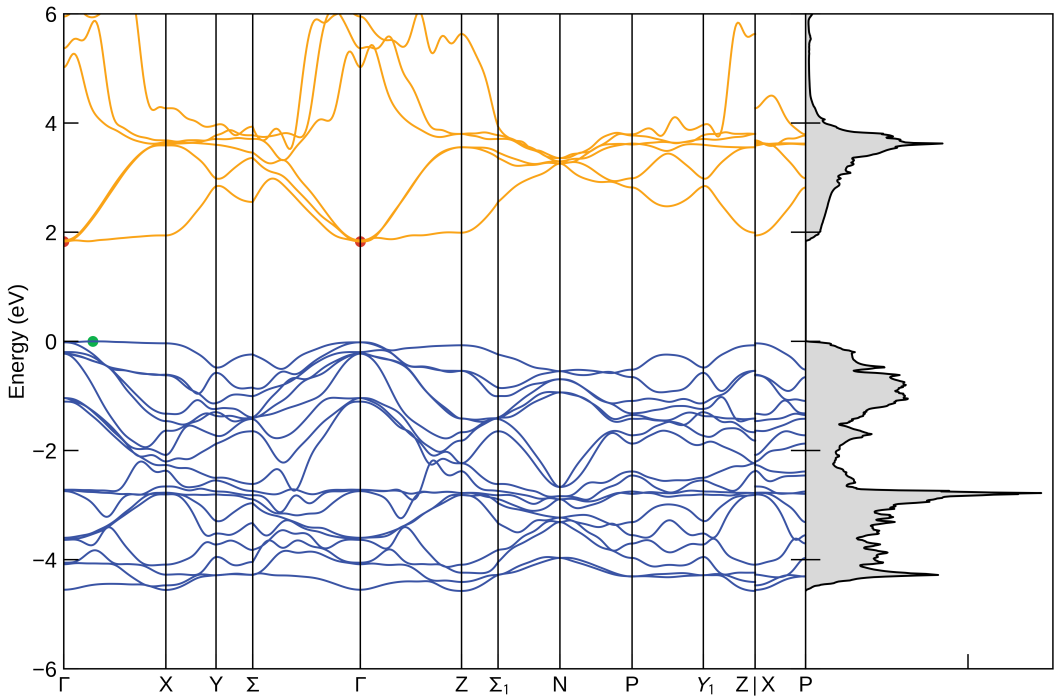

Fig. S8 Calculated electronic band structure and density of states (DoS) of $SrTiO_3$ obtained with the PBEsol exchange-correlation functional. The valence and conduction bands are shown in blue and orange, respectively, the valence-band maximum and conduction-band minimum (VBM/CBM) are marked by green and red circles, and the VBM is set to $E = 0$. Note that the PBEsol bandgap shown on these plots is smaller than the HSE06 values given in the paper.

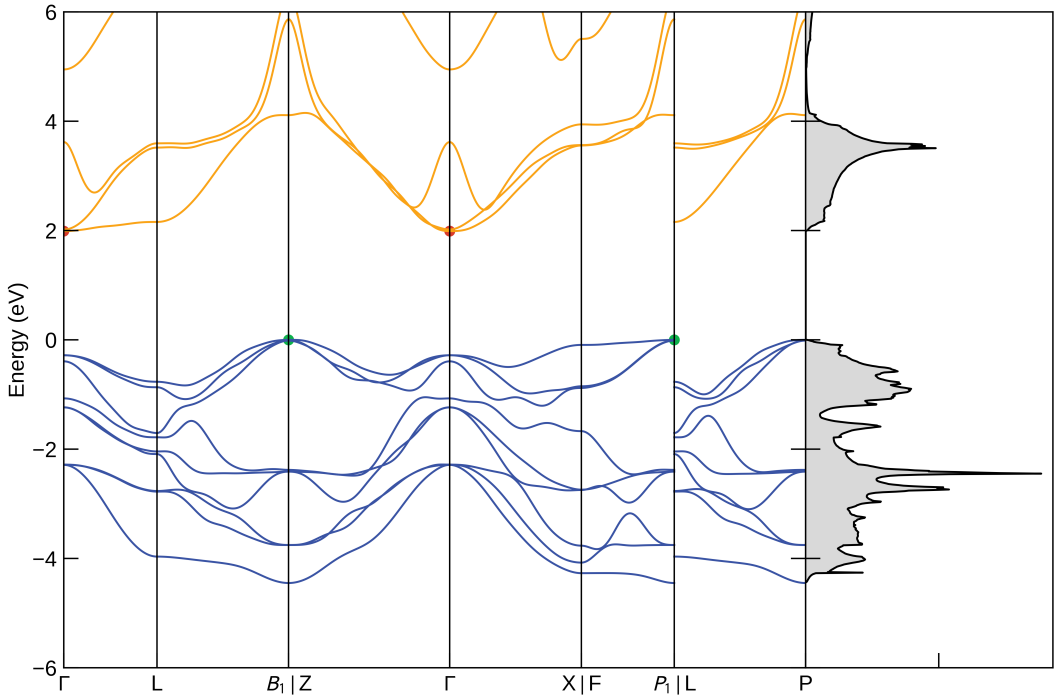

Fig. S9 Calculated electronic band structure and density of states (DoS) of $BaTiO_3$ obtained with the PBEsol exchange-correlation functional. The valence and conduction bands are shown in blue and orange, respectively, the valence-band maximum and conduction-band minimum (VBM/CBM) are marked by green and red circles, and the VBM is set to $E = 0$. Note that the PBEsol bandgap shown on these plots is smaller than the HSE06 values given in the paper.

2.3 Electron scattering rates

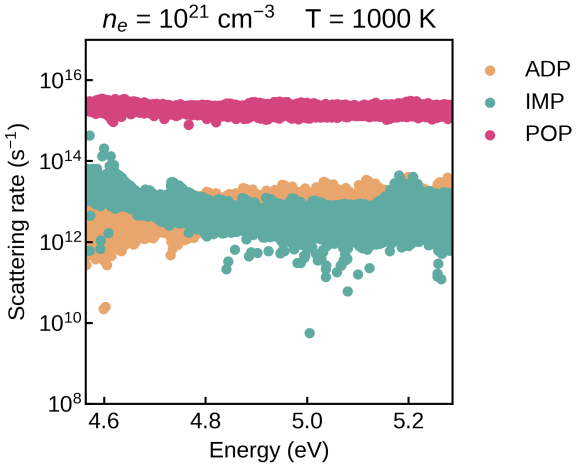

Fig. S10 Calculated electron scattering rates for $CaTiO_3$ as a function of energy in the vicinity of the conduction-band minimum (CBM) for a doping level $n = 10^{21}$ cm^{-3} and temperature $T = 1000$ K. The plot shows the separate contributions to the overall scattering rates from acoustic deformation potential (ADP), ionised impurity (IMP) and polar optic phonon (POP) scattering.

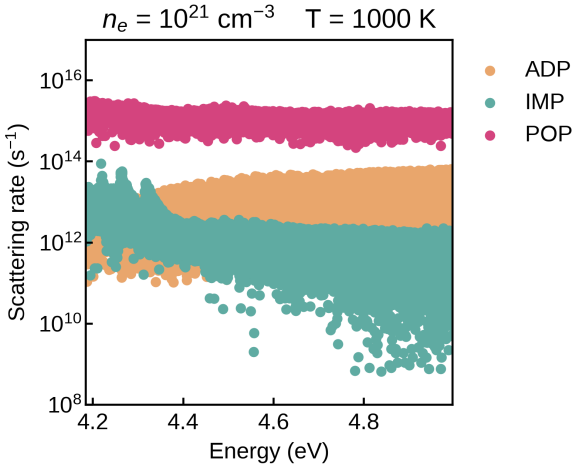

Fig. S11 Calculated electron scattering rates for $SrTiO_3$ as a function of energy in the vicinity of the conduction-band minimum (CBM) for a doping level $n = 10^{21}$ cm^{-3} and temperature $T = 1000$ K. The plot shows the separate contributions to the overall scattering rates from acoustic deformation potential (ADP), ionised impurity (IMP) and polar optic phonon (POP) scattering.

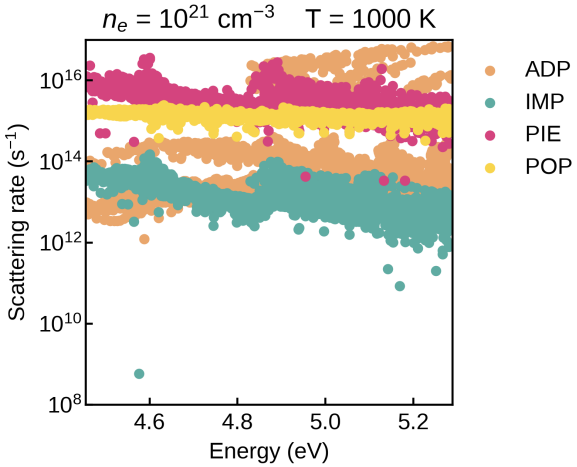

Fig. S12 Calculated electron scattering rates for $BaTiO_3$ as a function of energy in the vicinity of the conduction-band minimum (CBM) for a doping level $n = 10^{21}$ cm^{-3} and temperature $T = 1000$ K. The plot shows the separate contributions to the overall scattering rates from acoustic deformation potential (ADP), ionised impurity (IMP), piezoelectric (PIE) and polar optic phonon (POP) scattering.

2.4 Anisotropy in the electrical-transport properties

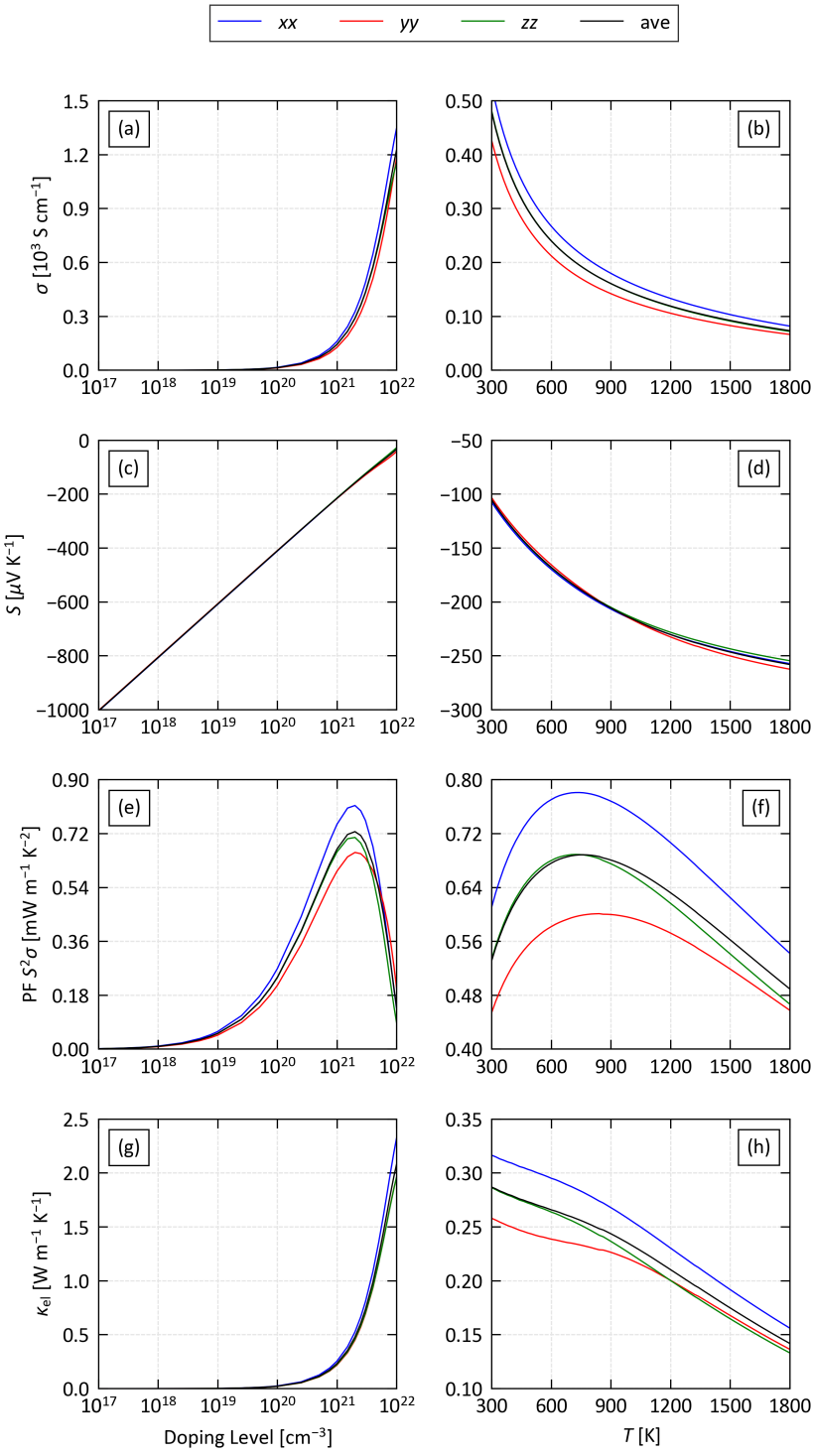

Fig. S13 Calculated electrical-transport properties of $CaTiO_3$: electrical conductivity σ (a/b), Seebeck coefficient S (c/d), thermoelectric power factor $S^2\sigma$ (PF; e/f) and electrical thermal conductivity κ_{el} (g/h). The four properties are shown as a function of doping level n at a fixed $T = 1000$ K (a, c, e, g), and as a function of temperature at a fixed $n = 10^{21}$ cm^{-3} (b, d, f, h). Each plot shows the principal xx, yy and zz elements of the tensors, together with the scalar averages $(xx+yy+zz)/3$ discussed in the manuscript.

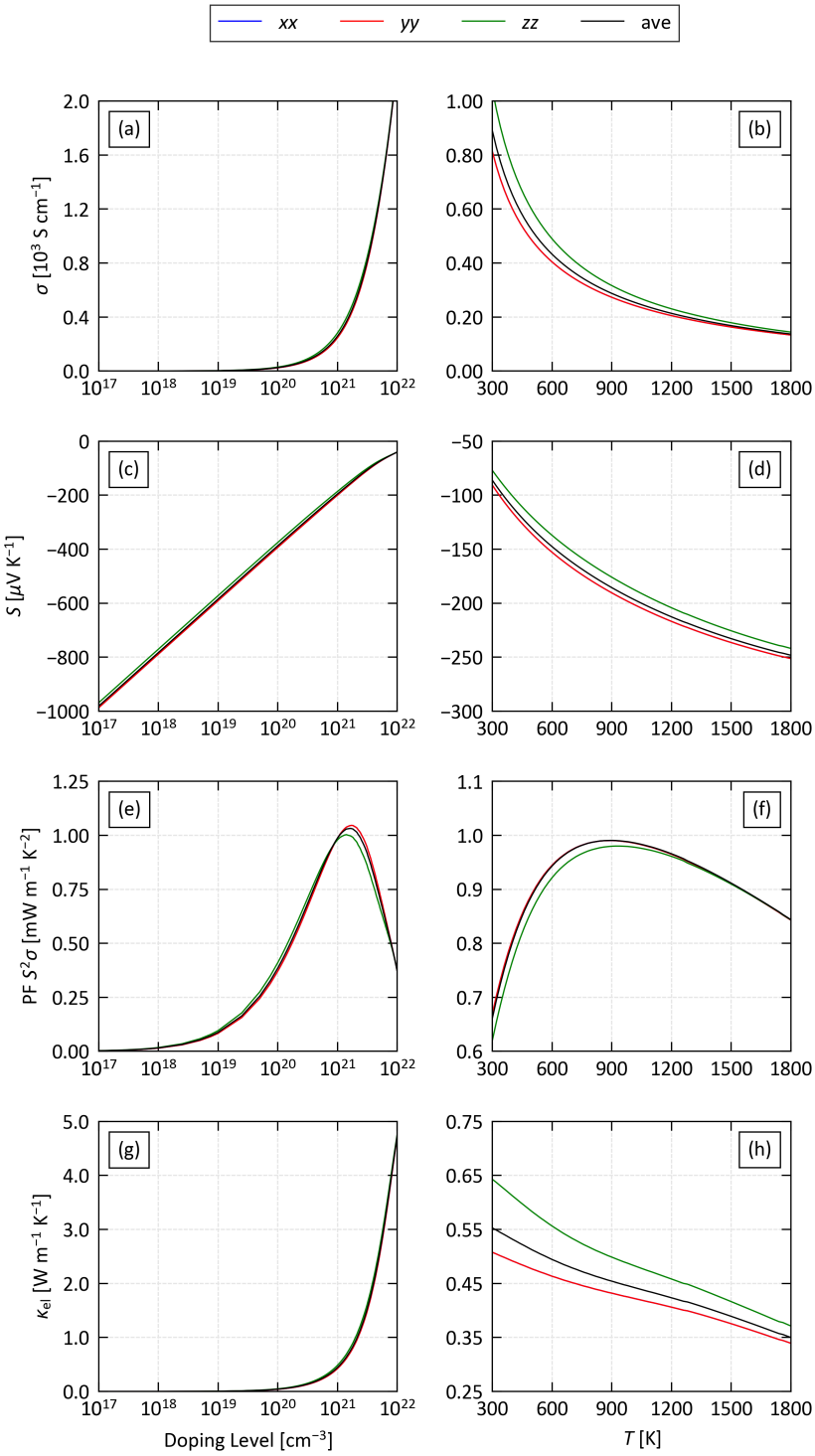

Fig. S14 Calculated electrical-transport properties of $SrTiO_3$: electrical conductivity σ (a/b), Seebeck coefficient S (c/d), thermoelectric power factor $S^2\sigma$ (PF; e/f) and electrical thermal conductivity κ_{el} (g/h). The four properties are shown as a function of doping level n at a fixed $T = 1000$ K (a, c, e, g), and as a function of temperature at a fixed $n = 10^{21}$ cm^{-3} (b, d, f, h). Each plot shows the principal xx, yy and zz elements of the tensors, together with the scalar averages $(xx+yy+zz)/3$ discussed in the manuscript.

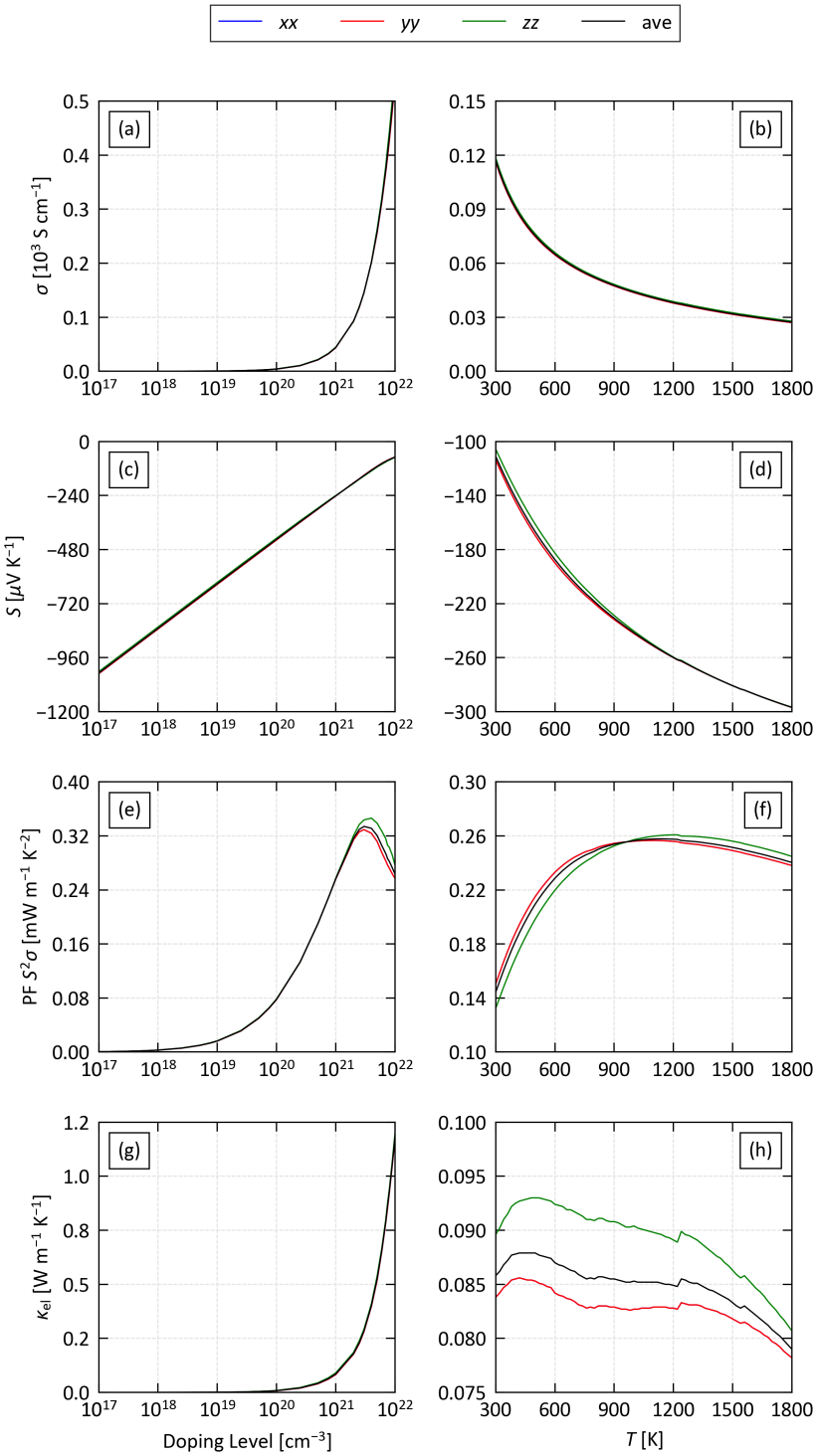

Fig. S15 Calculated electrical-transport properties of $BaTiO_3$: electrical conductivity σ (a/b), Seebeck coefficient S (c/d), thermoelectric power factor $S^2\sigma$ (PF; e/f) and electrical thermal conductivity κ_{el} (g/h). The four properties are shown as a function of doping level n at a fixed $T = 1000$ K (a, c, e, g), and as a function of temperature at a fixed $n = 10^{21}$ cm^{-3} (b, d, f, h). Each plot shows the principal xx, yy and zz elements of the tensors, together with the scalar averages $(xx+yy+zz)/3$ discussed in the manuscript.

2.5 Anisotropy in the thermoelectric figure of merit

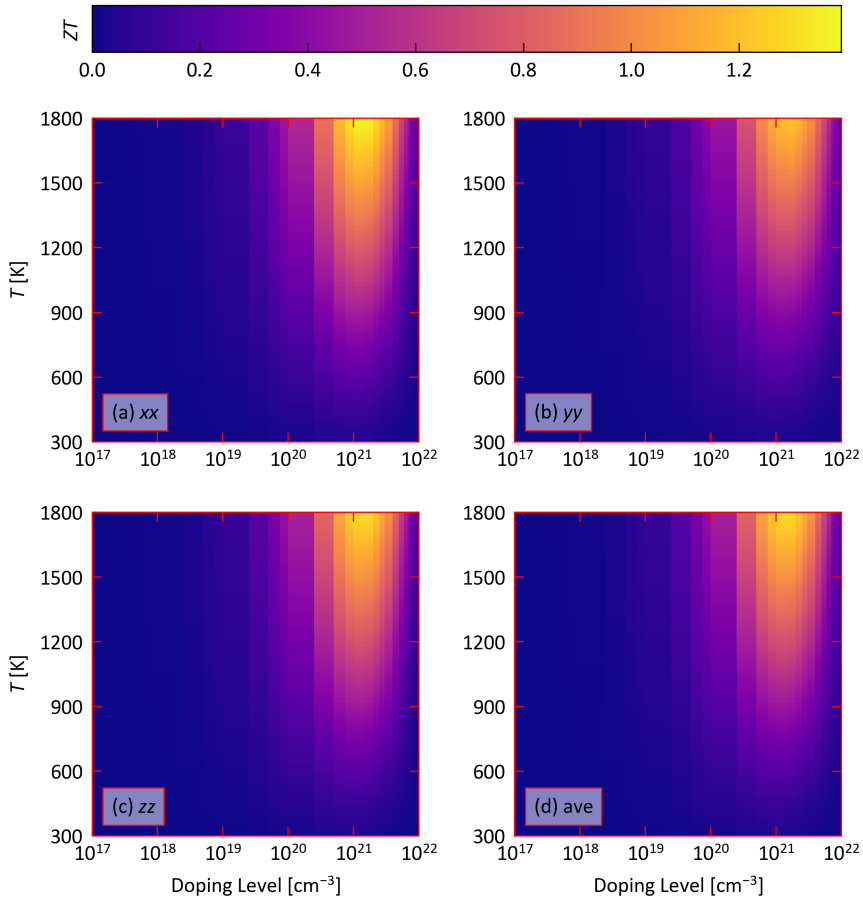

Fig. S16 Thermoelectric figure of merit of ZT $CaTiO_3$ as a function of doping level n and temperature. The four plots show the principal xx (a), yy (b) and zz (c) elements of the ZT tensors, together with the scalar averages $(xx+yy+zz)/3$ discussed in the manuscript (d).

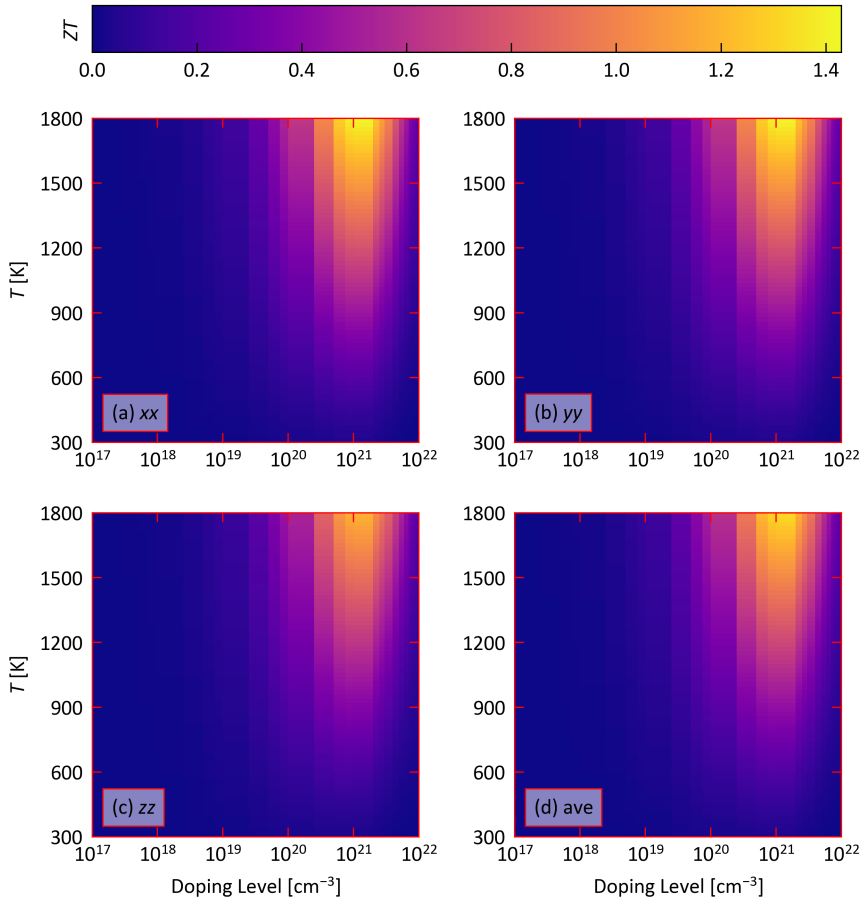

Fig. S17 Thermoelectric figure of merit of ZT $SrTiO_3$ as a function of doping level n and temperature. The four plots show the principal xx (a), yy (b) and zz (c) elements of the ZT tensors, together with the scalar averages $(xx+yy+zz)/3$ discussed in the manuscript (d).

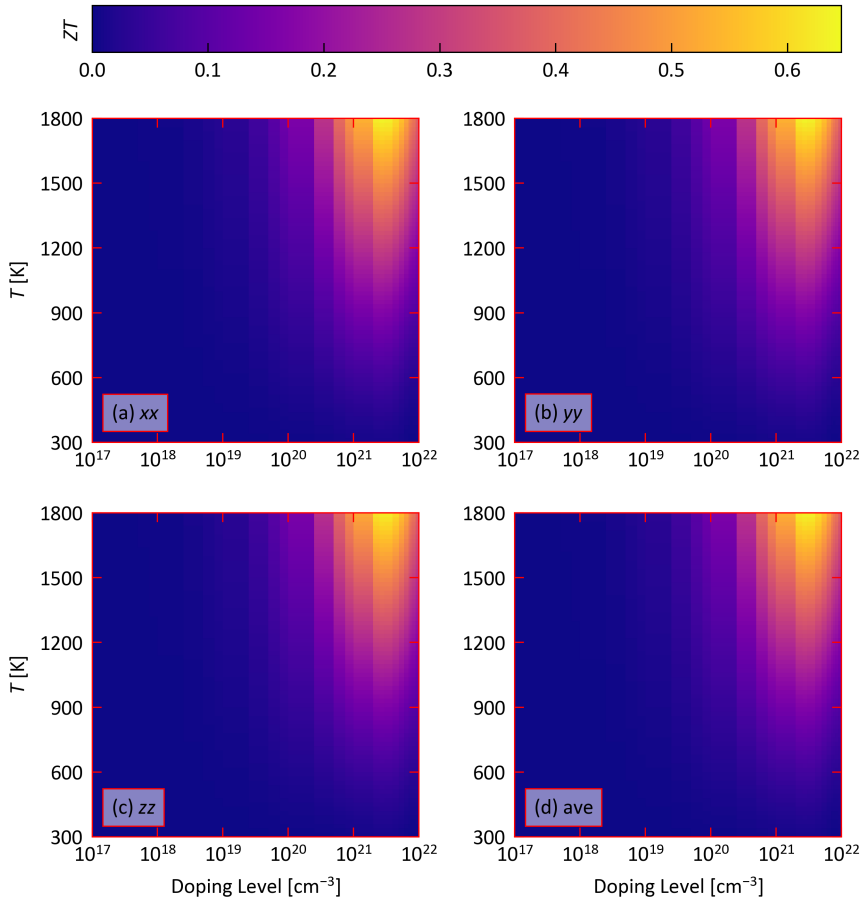

Fig. S18 Thermoelectric figure of merit of ZT $BaTiO_3$ as a function of doping level n and temperature. The four plots show the principal xx (a), yy (b) and zz (c) elements of the ZT tensors, together with the scalar averages $(xx+yy+zz)/3$ discussed in the manuscript (d).

1 S. Ohta, T. Nomura, H. Ohta and K. Koumoto, *J. Appl. Phys.*, 2005, **97**, 034106.

2 R. He, H. Wu, L. Zhang, X. Wang, F. Fu, S. Liu and Z. Zhong, *Phys. Rev. B*, 2022, **105**, 064104.

3 D. Narducci, E. Selezneva, G. Cerofolini, S. Frabboni and G. Ottaviani, *J. Solid State Chem.*, 2012, **193**, 19–25.

4 M.-S. Lee and S. D. Mahanti, *Phys. Rev. B*, 2012, **85**, 165149.